Paleoclimate controls on lithium enrichment in Great Basin Pliocene-Pleistocene lacustrine clays

Catherine A. Gagnon[1,2,†], Kristina L. Butler[3], Elizabeth Gaviria[1,4], Alexa Terrazas[5], Annabelle Gao[1], Tripti Bhattacharya[6], David F. Boutt[7], Lee Ann Munk[8], Daniel E. Ibarra[1,2]

[1]*Department of Earth, Environmental and Planetary Science, Brown University, Providence, RI 02912, USA*
[2]*Institute at Brown for Environment and Society, Brown University, Providence, RI 02912, USA*
[3]*Department of Geological Sciences, Jackson School of Geosciences, University of Texas at Austin, Austin, TX 78712, USA*
[4]*Department of Earth, Environmental and Planetary Sciences, Rice University, Houston, TX 77005, USA*
[5]*Department of Ocean and Atmospheric Sciences, University of California, Los Angeles, CA, 90095, USA*
[6]*Department of Earth Sciences, Syracuse University, Syracuse, NY 12344, USA*
[7]*Department of Geosciences, University of Massachusetts-Amherst, Amherst, MA 01003, USA*
[8]*Department of Geological Sciences, University of Alaska Anchorage, Anchorage, AK 99508, USA*

This manuscript has been submitted to *GSA Bulletin*. This paper is a non-peer reviewed preprint submitted to *EarthArXiv*. Subsequent version of this manuscript may have different content.

Paleoclimate controls on lithium enrichment in Great Basin Pliocene-Pleistocene lacustrine clays

Catherine A. Gagnon[1,2,†], Kristina L. Butler[3], Elizabeth Gaviria[1,4], Alexa Terrazas[5], Annabelle Gao[1], Tripti Bhattacharya[6], David F. Boutt[7], Lee Ann Munk[8], Daniel E. Ibarra[1,2]

[1]*Department of Earth, Environmental and Planetary Science, Brown University, Providence, RI 02912, USA*

[2]*Institute at Brown for Environment and Society, Brown University, Providence, RI 02912, USA*

[3]*Department of Geological Sciences, Jackson School of Geosciences, University of Texas at Austin, Austin, TX 78712, USA*

[4]*Department of Earth, Environmental and Planetary Sciences, Rice University, Houston, TX 77005, USA*

[5]*Department of Ocean and Atmospheric Sciences, University of California, Los Angeles, CA, 90095, USA*

[6]*Department of Earth Sciences, Syracuse University, Syracuse, NY 12344, USA*

[7]*Department of Geosciences, University of Massachusetts-Amherst, Amherst, MA 01003, USA*

[8]*Department of Geological Sciences, University of Alaska Anchorage, Anchorage, AK 99508, USA*

† Corresponding author: catherine_gagnon@brown.edu

ABSTRACT

Terminal lakes are important archives of continental hydroclimate and in some cases contain important economic resources. Here we present a ~2.9 million year lacustrine carbonate carbon and oxygen stable isotope record from a Great Basin continental drill core. We pair these measurements with bulk lithium concentrations to reveal a relationship between past climate and lithium enrichment in authigenic lacustrine clays. Further, we explore the possible effects of changing seasonality on the isotope record through the use of paired air mass trajectories and modern isotope data. Our findings show the evolution of the basin's moisture balance over million-year timescales, which we attribute to variations in precipitation seasonality as well as fluctuations in the amount of evaporation associated with changes in atmospheric moisture convergence and divergence. We observe a positive correlation between the oxygen isotope values of the lake carbonate and the bulk sediment lithium concentrations, which we argue is indicative of evapoconcentration of the lake environment and subsequent enrichment of the authigenic clays. Our results suggest a link between past hydroclimate changes and the formation of lithium-rich authigenic clays feeding high lithium concentrations in this modern brine aquifer system.

INTRODUCTION

Evidence from the relatively recent geologic past suggests that the Great Basin region of the western United States experienced enhanced moisture convergence in both warmer and colder climates compared to the modern (Matsubara and Howard, 2009; Salzmann et al., 2011; Pound et al., 2014; Ibarra et al., 2014; 2018; Lee et al., 2021; Fu et al., 2021). For example, the Last Glacial Maximum (LGM) was a vastly different climate state, with global sea level 140 m lower and global

mean annual temperatures ~6 ºC cooler than present (Clark et al., 2009; Annan and Hargreaves, 2013; Lora and Ibarra, 2019). During this time, the Great Basin sustained many pluvial lakes whose maximum extents represent a balance between precipitation and evaporative demand and suggest a much wetter environment (Mifflin and Wheat, 1979; Reheis, 1999; Orme, 2008; Kurth et al., 2011; Godsey et al., 2011; Munroe and Laabs, 2013; Ibarra et al., 2014; Reheis et al., 2014; Oster and Ibarra, 2018; Santi et al., 2020). A metric for evaluating the moisture balance of these pluvial lakes is precipitation minus evaporation (P-E), associated with regional atmospheric convergence (e.g., Lora and Ibarra, 2019), which we will use hereafter when referring to moisture balance. Similarly, the mid Pliocene (defined as ca. 2.9– 3.3 Ma for climate model simulations) experienced wetter-than-modern conditions in the southwestern United States (Pound et al., 2014; Ibarra et al., 2018; Fu et al., 2022). However, and in contrast to the LGM, a combination of proxies and modeling efforts suggest the late Pliocene global mean annual temperature was around 3.5°C warmer than today and had atmospheric CO_2 levels greater than pre-industrial (Ravelo et al., 2004; Dowsett and Gill, 2010; Burke et al., 2018; Haywood et al., 2020). Numerous hypotheses have been invoked to explain the wet conditions in the mid Pliocene. Some have proposed that weaker atmospheric circulation in response to the different ocean surface temperature patterns of the Pliocene reduced meridional and zonal temperature gradients (Molnar and Cane, 2002; Burls and Fedorov, 2017). Another recent hypothesis argues for more enhanced convergent monsoonal circulation developed over late boreal summer due to increased SST in the Pliocene (Fu et al., 2022). Lastly, strengthened southwesterly moisture delivery could have resulted in greater wintertime precipitation that fed the southwest USA lakes (Ibarra et al., 2018).

Lake basins in the Great Basin are important archives of climate, and in some cases, they also host significant economic resources (e.g., Davis and Gleason 1986; Munk et al., 2011; Bradley

et al., 2013; Castor and Henry, 2020). Clayton Valley (CV), Nevada is a long-lived Pliocene-Pleistocene lake basin and is also the location of the largest lithium brine resource in North America (Coffey et al., 2021). The availability of lithium is critical for the transition to renewable energy and electric vehicles because it is an important component of modern battery technology (e.g., Munk et al., 2016; Manthiram, 2017). In this study, deep sediment cores from CV allow us the opportunity to explore the intersection between Pliocene-Pleistocene hydroclimate change and the formation of this important resource. Additionally, the similarity between the climate state of the late Pliocene and today (Burke et al., 2018; Haywood et al., 2020), with minimal changes in continental configuration, orography, and paleogeography, make this lake basin an excellent case study for how regional hydroclimate in the southwestern United States might evolve in the future. In this study we address the following two key questions: *(1) How has the hydroclimate of CV varied during the late Pliocene to the Pleistocene? (2) What role does climate play in the formation of lithium rich clays in the CV Basin?*

To answer these questions, we present a new carbonate-based stable isotope hydroclimate record for CV, a terminal basin in the Great Basin of the western United States, and demonstrate through additional geochronology (cf. Coffey et al., 2021) that this basin contains lake deposits from the late Pliocene to late Pleistocene. We measured stable carbon and oxygen isotopes of carbonates from one of the previously described sediment cores (EXP2) and expand on the sedimentological interpretations of Coffey et al. (2021) to include thin section analysis and chemical weathering indices of alteration (CIA) based on bulk elemental analyses, as well as additional higher-resolution bulk lithium concentration measurements. Further, to provide a clear picture of the modern hydroclimate dynamics, we also include air mass back trajectory and analysis of precipitation for CV using the Hybrid Single-Particle Lagrangian Integrated

Trajectory model (HYSPLIT) (Stein et al., 2015; Warner, 2018). We compare these trajectories with nearby modern precipitation isotope data. Our results demonstrate that the long-term late Pliocene to late Pleistocene hydroclimate evolution from wet deep-lake conditions to increasingly desiccated and punctuated pluvial lake conditions greatly influenced lithium accumulation in this lacustrine clay deposit, which is the primary source of lithium to the modern brine aquifer system (Coffey et al., 2021).

SETTING

Clayton Valley is a topographically closed half-graben basin in Esmeralda County along the western margin of the Basin and Range Province about 80 miles to the northwest of Death Valley (M, Fig. 1). Fish Lake Valley (FLV) neighbors CV to the west. Basement fault blocks of Late Neoproterozoic to Ordovician, North American western passive margin, metamorphosed siliciclastic and carbonate units bound the basin on all sides. Surficial deposits consist of Tertiary volcanic and sedimentary rocks. During the late Paleozoic and Mesozoic the region underwent shortening and low grade-metamorphism. Since ~16 Ma the area has undergone continuous extension (Coffey et al., 2021; Oldow et al., 2009; Burrus, 2013). Clayton Valley lies at the northernmost extent of the North American Monsoon (NAM) (e.g., Ray et al, 2007; Means, 2013; Bhattacharya et al., 2017). The average annual precipitation is 13 cm (Munk and Chamberlain, 2011), which is delivered in the summer months by the NAM and in the winter months by westerlies. The valley floor playa spans 100 km^2 at an elevation of 1298 m. The entire topographic watershed for CV is 1,437 km^2 (Coffey et al., 2021). Recent groundwater flow modeling has shown a potential contribution from surrounding basins of upwards to 12,610 km^2 (Brooks et al., 2014; Underdown et al., 2017). Despite the large influence of interbasin flow (Fig.

1), the groundwater from all surrounding basins terminates in CV (Rush, 1968; Coffey et al., 2021). Water outflow is therefore limited to playa evaporation and evapotranspiration in the lowland areas of the valley where there is a shallow groundwater table.

MATERIALS AND METHODS

Core EXP2

The EXP2 core was one of five cores drilled in the CV basin between June 2017 and November 2017 by the Albemarle Corporation. The 3,250 ft (990.6 meter) long core was photographed and logged to the nearest tenth of a foot, with depths herein converted to meters.

From top to bottom, we summarize the major lithologic units after Coffey et al. (2021) (Fig 2). The upper clastic unit spans 0-228.6 m depth. The dominant sedimentology from 0-45.7 m consists of sands and gravels with interbedded clays, which transition to clays with thin infrequent sand interlayers from 45.7 m-228.6 m. The lower clastic unit spans 228.6-405.4 m, and primarily consists of brown and green clay with sparse interlayers of volcanic ash and silty clay. The clastic and salt unit is composed of thick layers of halite as much as 6.1 m thick with thin layers of clay in between from 405.4-535.0 m. The clastic and ash unit is next in succession from 535.0 m-896.7 m depth. This unit consists of green clay and thin volcanic ash layers with silt near the base of the unit. The remainder of the core below 897.7 m is angular gravel composed primarily of clasts of siltstone derived from the fault block mountains on the east side of the basin, this gravel unit overlies a Tertiary crystal lithic tuff which is also exposed on the east side of CV on Angel Island.

FLV Outcrop Samples

Fish Lake Valley outcrop samples were collected in the summer 2021 field season (Table S6) and measured for stable isotopes to compare to the CV record we generated. We visited the southeast playa and rimrock sections (Reheis et al., 1991, their Figures 2 & 4) as well as the northeast 179-EP section (Reheis et al., 1993; their Fig. 7). We attributed depths/heights to the outcrop samples relative to boundaries of units described by Reheis (1991, 1993). We then used a combination of previously dated ashes (Knott et al., 2018; 2019) and previously correlated magnetostratigraphy (Sarna-Wojcicki et al., 2005; their Fig. 15) following Mix et al. (2019) to assign ages (Tables S5 and S6). All reported age-depth relationships in the playa and badlands sections are estimations of contact points along the major lithologic units in the stratigraphic column.

Thin Sections

Thin section billets were cut and made into oriented standard size 30 micron-thick sections using a 600-mesh grit by Quality Thin Sections (Tucson, Arizona). No stains were applied. We imaged thin sections using an Zweiss Axio M2M microscope (Fig. 4) and under an optical microscope to assess the degree of alteration of lake carbonates.

Whole Rock Elemental Analyses and Lithium Concentrations

As in Coffey et al. (2021) whole rock samples were analyzed by SGS Environmental Services for whole rock geochemistry by X-ray fluorescence (XRF) and for lithium concentrations by Inductively Coupled Plasma Emission Spectrometry.

Briefly, approximately 1 gram of crushed and pulverized samples were formed into a homogenous glass disk by fusion with a lithium tetraborate/lithium metaborate mixture and then

analyzed by wavelength dispersion XRF (WD-XRF). All reporting limits are less than or equal to 0.01%. Calibration checks are performed daily. SGS methods conform to the ISO/IEC/17025. Lithium concentrations on solid samples were performed by ICP-OES by SGS. A 0.1 gram sample of crushed and pulverized sample was fused using Na_2O_2 and digested in HCl, and Li concentrations analyzed on an Agilent ICP-OES.

Dating Methods

In previous work Coffey et al. (2021) dated six ashes from the EXP cores using $^{40}Ar/^{39}Ar$ methods on sanidine. In this work we present two additional $^{40}Ar/^{39}Ar$ age and one zircon U-Pb ages to refine the age model for EXP2. For the new $^{40}Ar/^{39}Ar$ ages at 336.35 m and 774.8 m, sanidine and plagioclase (respectively) were isolated from the tephras via magnetic and density sorting techniques, and their composition was verified using a variable pressure scanning electron microscope. Separates were wrapped in aluminum foil, placed in 2.5 cm aluminum disks, and irradiated along with the 1.1864 Ma Alder Creek sanidine standard (Jicha et al., 2016) at the Oregon State University TRIGA reactor in the Cadmium-Line In-Core Irradiation Tube (CLICIT). Single crystal fusion experiments were performed with a 50 W CO_2 laser in the WiscAr laboratory at the University of Wisconsin-Madison. Gas was analyzed using a Noblesse multi-collector mass spectrometer using the procedures in Jicha et al. (2016). Weighted mean ages are calculated using the decay constants of Min et al. (2000) and are reported with analytical uncertainties at the 95% confidence level. Atmospheric argon value used is that of Lee et al. (2006). Weighted mean average and relative probability plots are included in Fig. 3.

One volcanic ash sample (EXP2_3277) was collected from EXP2 drill core for zircon U-Pb crystallization age at a depth of 998.8 m. Zircon grains were isolated by traditional physical

and chemical mineral separation methods, including crushing, grinding, and hydraulic, heavy-liquid, and magnetic separation. Zircon grains were then poured onto double-sided tape on epoxy resin mounts and 33 inclusion-free zircons were selected for U-Pb analysis by laser ablation–inductively coupled plasma–mass spectrometry (LA-ICP-MS) at the University of Texas at Austin. Mounts were transferred to a large-volume Helex sample cell and analyzed by a magnetic sector, single collector Element2 HR-ICP-MS with an attached PhotonMachine Analyte G.2 Excimer Laser ablation system. Data reduction was performed in the Iolite software (Paton et al., 2011). A weighted mean average age (6.134 ± 0.095 Ma) was calculated from a unimodal youngest population of 16 zircon ages, resulting in an MSWD of 0.78. Ages with discordance >30% were excluded from the age calculation as well as ages clearly defining older age populations (i.e. inherited zircons). Weight Mean Average plot and Whetherill Concordia were constructed using IsoplotR (Fig. 3; Vermeesch, 2018). See Table S3 for zircon U-Pb analytical results.

Age-Depth Model

The hydroclimate interpretation for CV relies significantly on the time evolution of oxygen and carbon isotopes along with the sedimentology of the core. We constructed a *rbacon* (Blaauw, M., & Christen, 2011) age-depth model (Fig. 2) and assigned mean ages to all samples based on the five $^{40}Ar/^{39}Ar$ ages that span the stable isotope dataset (Table S1). We have chosen to not include the U-Pb age in the model, since the sample depth is so far beneath the lacustrine sequence where all our stable isotope measurements were made. We modeled the top of the core to be Holocene in age, 5ka +/- 5ka. Since our isotope record does not extend into the alluvial fan deposits, we have chosen to cut off our age model at the interface between these coarse deposits and the silt deposits to avoid extrapolating over major changes in lithology. We used the "slump"

command in *rbacon* to account for geologically instantaneous deposition of the Bishop Tuff and other ash layers. Additionally, in the supplement we present the age model using the "slump" command in *rbacon* for each of the halite deposits, which we believe were deposited more rapidly than the overlying and underlying fine clays.

Stable Isotope Analyses

A total of 285 carbonate samples from EXP2 were measured for $\delta^{18}O$ and $\delta^{13}C$. The stable isotope measurements were made on one of three instruments– Thermo Finnigan MAT 252 with a Kiel III at Brown University, Thermo Finnigan MAT 253+ with a Kiel IV at Brown University, or a Thermo Finnegan Deltaplus XL with a gasbench at Stanford University (Table S2), with replication across laboratories and mass spectrometers. Carbonate stable isotope ratios are reported using standard δ-notation relative to the VPDB standard.

The samples that were analyzed at Brown University were first dried overnight at 60 ºC, then homogenized via mortar and pestle. Of the sample, 500 μg were weighed out and reacted with 70 degree C phosphoric acid using a Thermo Finnigan Kiel III or Kiel IV carbonate device. This measured weight is based on a typical 10% sample carbonate content and a required 50 micrograms of CaCO3 for the desired range of measurement voltage (3 to 6 V). The evolved CO2 was measured on either a Thermo Finnigan MAT 252 gas-ratio mass spectrometer or Thermo Finnigan MAT 253+ (Table S2). External precision (1σ) of oxygen and carbon isotope data is <0.1‰, based upon repeated measurements of two internal laboratory standards, BYM63150 and Carrara63150, calibrated against NBS 18, NBS 19, and IAEA 603.

The samples that were analyzed at Stanford University in 2018 were homogenized via mortar and pestle. Stable carbon and oxygen isotope values of carbonates were obtained at the

232 Stable Isotope Biogeochemistry Laboratory, Stanford University, using a Thermo Finnigan
233 Gasbench and measured on a Finnigan MAT Delta+ XL mass spectrometer using a Thermo
234 Finnigan ConFlo III unit. Approximately 300 μg of sample powder was weighed into sealed
235 vials that were flushed with helium gas and reacted with ca. 0.25 ml of phosphoric acid (H3PO4)
236 for 1 hour at 72°C. External precision (1σ) of oxygen and carbon isotope data is <0.1‰, based
237 upon repeated measurements of two internal laboratory standards calibrated against NBS 18,
238 NBS 19, and LSVEC.
239 We calculated a running correlation coefficient (R) for the entire $\delta^{18}O$ and $\delta^{13}C$ record
240 using the *movcorr* function in MATLAB. This function calculates a running R value for a
241 moving window of data points. For our record, we used a 5-pt moving window and plotted the
242 resulting R value in Fig. 5.
243
244 *Precipitation Back-Trajectory Analyses*
245 To understand the influence of seasonality and moisture source on our oxygen isotope
246 record, we modeled the moisture source trajectories entering CV, and paired these with modern
247 water oxygen isotopes. Back-trajectories were generated using the desktop version of the Hybrid
248 Single-Particle Lagrangian Integrated Trajectory (HYSPLIT) model and the North American
249 Regional Reanalysis (NARR) as the HYSPLIT meteorological input. We tracked air parcels
250 backwards for 72 hours every 24 hours at 1500 meters above ground level to gauge the
251 precipitation sources of each of the study sites. Daily 72 hour back-trajectories began at the end
252 of the day and were generated for every day between 1979-2019, which covers the extent of the
253 NARR climate record.

In order to filter trajectories by precipitation events, we used weather station data in the Global Historical Climatology Network-Daily (GHCN-D) database, keeping both geographical location and elevation as close as possible. The station record from Silver Peak, NV (within CV) records historic snow and rain events throughout 1979-2019, both of which are considered in our precipitation analyses. For each site, trajectories were matched with the corresponding day in the meteorological record and filtered based on whether there was any rain or snow for that day. Days that were missing both a rain and snow record were not included in the analyses. The resulting precipitation trajectories were then filtered by summer (April-September) and winter (October-March) half year months.

Once the precipitation-carrying trajectories were filtered, a cluster analysis was completed for each site's summer, and winter trajectories using HYSPLIT's built-in clustering program. The number of clusters in each analysis was determined by the change in Total Spatial Variance (TSV) curve generated as clusters were combined. The point at which the fewest number of clusters had a change in TSV less than about 15% was selected for the analysis. The trajectories in each cluster were then averaged and plotted on a map with a topographic overlay. Finally, we weighted the cluster means by total precipitation delivered. The thickness of the lines on Fig. 6 are scaled to this weighting.

A similar set of HYSPLIT analyses (without clustering) was conducted for weekly precipitation samples from the NV00 site at Red Rock Canyon (36.13483 ºN, -115.422 ºW, 1,137 m) from the USNIP network (Welker, 2012), the closest site to CV. Shown on Figure 2A are daily trajectories for all days with precipitation colored by the oxygen isotope value of the weekly aggregated rainfall. This station contains data spanning May 1989 to December 1994, with 29 total weeks of isotope data.

RESULTS AND DISCUSSION

New ash ages

In previous work Coffey et al. (2021) dated six ashes from the EXP cores using $^{40}Ar/^{39}Ar$ methods on sanidine. In this work we presented two additional $^{40}Ar/^{39}Ar$ ages and one zircon U-Pb age to refine the age model for EXP2. Sample EXP2_1103-1104 was collected at 336.35 m depth. A weighted mean average age of 1145.7 ± 10.8 ka (MSWD = 0.93) was calculated from 17 of 25 dated sanidine crystals (Fig. 3). Sample EXP2_2542 was collected at 774.8 m depth. A weighted mean average age of 2.476 ± 0.068 Ma (MSWD = 1.12) was calculated from 17 of 25 dated plagioclase crystals (Fig. 3). We present a new U-Pb zircon age from an ash at 998.8 m depth in the EXP2 core, sample EXP2_3277. The youngest coherent population of 16 of the 33 dated zircons were selected to calculate a weighted mean average age of 6.134 ± 0.095 Ma (Fig. 3). The remaining 16 zircon ages define older age populations (interpreted to be inherited zircon crystals) or were filtered out with our discordance filters (see Methods section). We note here that the U-Pb age matches a K-Ar age on a rhyolite flow that is well exposed in the Silver Peak Range to the east (Robinson et al., 1968, GSA Memoir 116).

Age-Depth Model

The age-depth model for EXP2 is relatively linear, with a larger uncertainty near the base of the lacustrine sequence (Fig. 2). The model only extends to the top of the alluvial fan deposits (~896.7 m), since we have very little age control into these coarser units. We suspect some change in sedimentation rate across this boundary, and therefore do not feel justified in extrapolating the above sedimentation rate into the base of the core. All lacustrine samples were

assigned mean *rbacon* ages (Table S2). The bottom most silt/clay deposits overlying the basal alluvial fan deposits are modeled to be 2900 ka, while the topmost sample is approximately 20 ka. This age for the bottom of the lacustrine sequence makes sense, considering that there are thick, slightly older tephra deposits in FLV which do not appear in EXP2 (Reheis, 1991, 1992; Reheis and others, 1993; Sarna-Wojcicki et al., 2005).

We suspect that the halite deposits were laid down at a faster rate than the clay deposits in a drying environment, which would shift the ages below the halite section but above the ashes dated below the halite section to be slightly younger. To get a minimum age estimate on our samples due to varied sedimentation rate, we explored the effects of modeling the halite beds as slumps. We found that the bottom most silt/clay deposits become 2850 ka with the added slumps, which is within error of the model run used to assign ages.

Depositional System in CV

The stratigraphic succession of the EXP2 core is typical of an underfilled to balance-filled lake in an extensional basin setting (e.g., Carroll and Bohacs, 1999; Ingersoll, 2012). Assuming no hiatuses, the sedimentation rate appears to be relatively linear throughout with the possibility of some variance towards the bottom of the core where we have little age control and a transition from clays to coarser grained material.

Based on the sedimentology we describe the depositional system. Starting at ~2900 ka, CV especially held a deep lake, evident from the thick green laminated lacustrine muds which persisted intermittently until the late Pleistocene with the youngest lacustrine muds at ~20 ka. The base of the record begins at 2900 ka as a deep lake. Thick halite beds abruptly punctuate the lacustrine deposits between 1750 ka-1380 ka before becoming a deep lake again. These halite

beds likely represent rapid changes in the moisture balance for the CV area. We interpret this point in time to be a perennial saline/mudflat environment. This change in the moisture budget is also supported by a notable transition in the degree of weathering from high to low, such that we start to see less weathered material in the core above the halite section, which persists until increasing again around 800 ka (Fig. S2). Around 780 ka, the record transitions from a deep lake to a shallow lake environment. At ~60 ka, the sediments coarsen upward in the section, signifying a gradual transition from a long-standing lake to the more arid playa environment, consistent with no significant LGM lake above the playa being present in this basin (Reheis, 1999). The uppermost coarse-grained sediments in EXP2 are more difficult to interpret, due to the poor core recovery, so it is unclear when the playa lake became permanently desiccated, we infer this to be ~23 ka, which corresponds to the youngest carbonate sample recovered. Further, in the neighboring valley to the west, Fish Lake Valley, there is no evidence for a large LGM (~21 ka) lake. Pluvial Lake Rennie existed in FLV 2.0 Ma until after 0.77 Ma when Lake Rennie was either contiguous with a lake to the north in Columbus Salt Marsh or it overflowed into FLV. After, Lake Rennie was dry or maintained very low levels from 0.5 Ma to the present (Reheis et al., 1993; Kurth et al., 2011).

Stable Isotope Results

The $\delta^{18}O$ values range from -14.1‰ to +4.6‰ (Fig. 5). The $\delta^{13}C$ values range from -8.0‰ to +5.4 (Fig. 5; Table S2). The running correlation coefficient between $\delta^{13}C$ and $\delta^{18}O$ shows a strong positive correlation for much of the timeseries, confirming as expected, that the basin was closed and terminal throughout its existence (Li et al., 1997; Leng and Marshall, 2004). The running standard deviation of $\delta^{18}O$ from 2 Ma to 20 ka increases by a factor of 2

346 relative to the pre-2 Ma samples (Fig. S2). This is likely related to the onset of Northern
347 Hemisphere glaciation and the intensification of glacial-interglacial cycles during the
348 Pleistocene. There is also a gradual positive shift of about 10‰ in the oxygen isotopes from the
349 base of the core to around 2 Ma l (Fig. 5). From 2 Ma to about 20 ka, there is a long-term
350 negative trend in the oxygen isotopes of about 10‰.

351 There are three hypotheses that may explain the long-term trend we observe from the late
352 Pliocene to present. First, Quaternary uplift in the White Mountains and Sierra Nevada and
353 subsequent blocking of winter moisture derived from the west of CV could have led to further
354 depletion of source $\delta^{18}O$ via orographic effects (Lechler and Galewsky, 2013; Mix et al., 2019;
355 Hildreth et al., 2021). Second, changes in precipitation seasonality from summer precipitation to
356 winter precipitation could drive source water $\delta^{18}O$ towards progressively depleted values. For
357 example, this would entail the addition of moisture from a more northerly source during colder
358 glacial periods rather than the central Pacific (Oster et al., 2020; discussed further below). Both
359 changes in orographic rainout due to topographic changes or changes in seasonality would
360 primarily influence the light endmembers in the observed oxygen isotope timeseries. Lastly, a
361 gradual decrease in temperature through the Pleistocene and subsequent reduction in the
362 effective evaporation could also lead to a more depleted lake water composition (i.e., more
363 overall P-E). This effect would influence the declining average and the range in the observed
364 oxygen isotope timeseries. Because of the evaporative nature of lacustrine carbonate oxygen
365 isotope records, we cannot necessarily rule out any of these scenarios with existing data.
366 However, as described in the next section, data from adjacent basins with differential
367 evaporation suggest that further orographic rainout can be ruled out (first scenario above
368 associated with Quaternary uplift of the White Mountains and Sierra Nevada). Further, we can

rule out an additional alternate scenario that changes in carbonate formation temperature (i.e., lake water temperature) influence our observations. Long term cooling would cause an increase not a decrease in the carbonate $\delta^{18}O$ values towards the present because of a larger fractionation factor between lake water and carbon at decreasing temperatures (Kim and O'Neil, 1997).

Comparison to Regional Records

There are multiple records of pluvial lakes in the region surrounding CV ranging in age from the late Pliocene to the late Pleistocene. These records indicate a different regional moisture balance for this area of the Great Basin relative to today. The lake stages shown on Fig. 5, adapted from Knott et al. (2019), shows the interpreted lake stages for CV and nearby lakes. Pluvial lakes in Death Valley (Lake Manly) (Lowenstein et al., 1999; Forester et al., 2005; Knott et al., 2018), to the south in Searles Valley (Smith et al., 1983; Jannik et al., 1991; Knott et al., 2018), and in Eureka Valley (Lake Andrei) began to form ~3.5–3.4 Ma in the late Pliocene during the cooler, wetter, glacial climate of MIS MG5 (Knott et al., 2019). The Death Valley lake persisted until ~3.30 Ma, while Searles lake persisted through the start of Northern Hemisphere glaciation until about 2.5 Ma. Lake Andrei was very short-lived, existing for only around 400,000 years (Knott et. al, 2019). Evidence from FLV suggests a lake existed from ca. 3.4 to 2.8 Ma (Reheis et al., 1993; Reheis et al., 2002; Knott et al., 2018). Lakes in these areas also existed intermittently during the Pleistocene. Pluvial lakes in Death Valley formed again ~1.98–1.78 Ma, 1.3–1.0 Ma, and ca. 0.6 Ma, while Searles Lake existed from about 2 Ma to the late Pleistocene. Fish Lake Valley episodically sustained a lake in the middle Pleistocene ~2.2-0.7 Ma. A potential record also exists for Owens Valley (0.8 Ma to the late Pleistocene) (Smith

et al., 1997) and also ~2.6-2.0 Ma, as recorded in the Waucobi lake beds (Sarna-Wojcicki et al., 2005; DeMasi et al., 2013; DeMasi et al., 2017).

Modern back trajectory analyses for CV show the area receiving different sources of water vapor depending on the season (Fig. 3). Winter parcels have a more northwesterly origin, tend to originate from more distant sources, and usually pass over the southern Sierras and White mountains. Summer trajectories originate from southerly areas, such as the Gulf of California and divert around the high relief to the west. Modern meteoric water $\delta^{18}O$ are also shown to have different compositions depending on the season (Fig 7).

We interpret the lightest $\delta^{18}O$ values at a given time slice in our record to represent meteoric water values (e.g., Rowley and Currie, 2006; Caves et al., 2017). Different seasonal source signals could impact the source water composition of the lake in CV directly impacting the light $\delta^{18}O$ endmember of our record. Therefore, we argue that the majority of the variance in the isotope record for CV is controlled by changes in seasonality and subsequent evaporative enrichment. Specifically, through the latest Pliocene there is a shift to more summertime precipitation events characterized by high $\delta^{18}O$ values, likely related to an enhancement of the convergent monsoonal circulation. Through the Pleistocene, we observe a very gradual decrease in light $\delta^{18}O$ endmember values, which we attribute to the weakening of monsoonal circulation, and strengthened southwesterly moisture delivery of wintertime precipitation. Our interpretation of the light $\delta^{18}O$ endmember is subject to uncertainty because it is difficult to disentangle changes in the meteoric water composition relative to changes in evaporation. As such, future work analyzing the leaf wax δD from CV may help isolate the meteoric signal.

Stable isotope evidence from the neighboring FLV (Fig. 1, Fig. 8) demonstrates a different water balance than CV, which complicates our interpretation that source changes are

414 responsible for the long-term trends in $\delta^{18}O$. If both records were dominated by source changes,
415 the $\delta^{18}O$ would have a consistent slight offset between them, since they are geographically
416 proximal. Further, lake stage transitions between basins were asynchronous as well, suggesting a
417 different water balance between basins. We explored the possibility that these asynchronous
418 changes in lake stage could be linked to uplift in the White Mountains and Sierra Nevada west of
419 FLV. Blocking of westerly moisture (Mix et al., 2019) could potentially have led to FLV drying
420 prior to CV (Reheis et al., 1993), which is why a shallow lake is observed for CV after FLV
421 desiccated (by ~0.6 Ma). In this case, we would expect to see progressively more depletion in
422 oxygen isotopes as moisture moves eastward encountering subsequent orographic rainout, into
423 FLV, then into CV. The oxygen isotope record generated for FLV (*this study*; Mix et al., 2019)
424 discredits this hypothesis, as the lightest endmember values of $\delta^{18}O$ of FLV are more depleted
425 than that of CV (Fig. 8). Further, ~0.6-0.7 Ma coincides with the integration of FLV and the
426 Columbus Salt Marsh (Reheis et al., 1993), which suggests that changes in basin hydrology-not
427 climate or tectonics-may be responsible for asynchronous changes in lake stage between the
428 neighboring valleys.
429
430 *Hydroclimate controls on lithium enrichment*
431 The lithium concentrations in the clays are one to two orders of magnitude greater than
432 that of the average continental crust (Fig. 5), 35 ± 11 ppm (Teng et al., 2004). There is no
433 statistical correlation between lithium and sediment age. However, there is a distinct positive
434 logarithmic correlation ($R^2 = 0.56$) between the paired measurements of lithium concentrations
435 and carbonate $\delta^{18}O$ (Fig. 9A).

436 We draw from Coffey et al. (2021) for the conceptual model for lithium brine
437 development in basins like CV. Geothermal fluids rich in lithium interact with the basin
438 sediment. For example, results from Araoka et al. (2014) indicate that the lithium concentrated in
439 playas in Nevada was supplied mainly through high-temperature water–rock interaction
440 associated with local geothermal activity and not directly by low-temperature weathering of
441 surface materials. However, over long periods of time water-rock interaction in the CV aquifer
442 allows Li and other solutes to accumulate in pore spaces. These high solute pore waters over
443 time move from high pressure (deeper) to lower pressure (shallower) zones in the aquifer which
444 is part of the brine forming process. Basin sediments can adsorb lithium, until groundwater
445 liberates the adsorbed lithium into the shallow subsurface waters. The lithium then becomes
446 concentrated in the shallow subsurface brines through evapoconcentration. The findings of this
447 study bear on the initial lithium enrichment of the basin sediments and link them to the
448 hydroclimate evolution of the basin and lake system over the Pliocene-Pleistocene.
449 We argue that our new observations showing a covariance between the authigenic
450 carbonate $\delta^{18}O$ in the lacustrine clays and the bulk lithium concentrations (Fig. 9) is related to the
451 degree of evapoconcentration of the lake during authigenic clay and carbonate precipitation in
452 the lake water. Variations in the past surface area to volume ratio of the lake could have an
453 impact on the degree of effective evapoconcentration of the lake water. For example, early in the
454 record (~2.9 to ~1.8 ka), as indicated by the CIA values and sedimentology (Fig. S2), P-E was
455 relatively large, the lake was deep, and the surface area to volume ratio of the lake was likely
456 smaller. This deep lake persisted until the onset of halite deposition. The climate then
457 transitioned at ~1.8 ka to a lower P-E, the lake became smaller and frequently desiccated. Due to
458 the higher surface area to volume ratio of the shallower lake, there was highly effective

evaporation that concentrated lithium in the lake. We propose that the lithium is then incorporated into the structure and onto the surfaces of the authigenic clays precipitating in the lake water. Additionally, a survey of brine samples (Fig. 9B) from the basin demonstrates a similar logarithmic relationship between water $\delta^{18}O$ and brine lithium concentrations (*This Study;* Coffey et al., 2021) compared to the geologic EXP2 samples shown in Figure 9A.

Evaporation plays a dominant role in the concentration of Li in both the brine and clay deposits, however ongoing work will better clarify the Li mass balance of the basin. While surface weathering of volcanic rocks may contribute Li to the lake, these fluxes are likely small across the topographic watershed. We speculate that a combination of groundwater with long transport pathways draining from neighboring landscapes (Brooks et al., 2014; Underdown et al, 2017), surface weathering, and hot springs in the north, west, and south parts of the basin (deposits observed by Coffey et al., 2021) contributed Li into the lake in CV. Very high lithium concentrations (1000s ppm) are reported in lacustrine clay deposits recently explored in the Tonopah basin (Loveday et al., 2020) to the northeast of CV. This region is hydraulically up-gradient of CV therefore we hypothesize that some of the Li is transported by interbasin groundwaters.

Primary versus Secondary Mineralization

There is a question of whether the Li became incorporated into the clays after deposition due to geothermal interactions, or if the clays incorporated the lithium during initial genesis in the lake water (Kunasz 1974; Davis, 1981; Morissette, 2012; Coffey et al., 2021). Our paleoclimate and Li-enrichment conceptual model interpretations rely on the assumption that most of the bulk sediment carbonates and clays are primary authigenic minerals. We base this

assumption on: (1) qualitative analysis of thin section images, and (2) prior XRD work conducted by Morissette (2012) and Coffey et al. (2021).

Four thin sections taken at 283 m, 308 m, 767 m, and 892 m (Fig. 4) support our assumption that the carbonate minerals within the sediments are primarily authigenic. The carbonate minerals within all four thin sections have a homogeneous micritic texture within an even beige to grey-green clay matrix. There appears to be no dissolution features, rimming cements, or syolititc features present in any of the images, which are all features that would likely be present if the sediments experienced significant post-depositional alteration. The 308 m and 767 m thin sections have lighter beige features, which are due to uneven sample thickness on the thin section mount (Figure 4, B and C).

Previous mineralogical work suggests the clay minerals also may be authigenic. Substantial Li deposits tend to be found within three different clay mineral types—smectite, illite, and montmorillonite (Morissette, 2012; Castor et al., 2020; Li et al., 2021; Coffey et al., 2022). Coffey et al. (2021) claim that the bulk sediments could be hectorite, which contains Li in the octahedral layer of trioctahedral smectite in place of Mg or more loosely held in the interlayer sites. Hectorite is thought to occur in several ways: (1) precipitation in alkaline lake deposits (Starkey, 1982; Calvo et al., 1999); (2) alteration of volcanic glass under hydrothermal and low temperatures; and (3) incorporation of Li into pre-existing smectite (Starkey, 1982; Kloprogge et al., 1999; Coffey et al., 2021). We argue that (1) is the dominant mechanism for Li enrichment at this site based on prior interpretations and thin section work presented in this study. Locally where volcanic ash was deposited into the lake there was likely some alteration of the ash to release solutes including Li, but this would introduce Li to the lake at punctuated times and the alteration would be confined to near the ash layers. Davis (1981) hypothesized that the

hectorite was precipitated from lake waters or pore fluids during early burial diagenesis in the CV basin. The case for authigenic hectorite is further supported by the leach experiments performed by Coffey et al. (2021), which indicate that a large fraction of the Li is contained in more difficult to dissolve silicate structures rather than on the more exchangeable interlayer surfaces of the clays. Ongoing work will shed light on the conditions for clay and carbonate formation--whether authigenic precipitation or hydrothermal alteration of existing smectites--and ultimately refine our understanding of the Li-brine system in CV as a whole.

Based on the evidence above, and the covariance between $\delta^{18}O$ and lithium concentrations (Fig. 9A) we argue that the bulk of lithium enrichment occurred at the time of clay mineralization in equilibrium with the lake water, and not post-depositionally. Future work analyzing the oxygen, hydrogen, and lithium isotopes of clay fractions from EXP2 may demonstrate this link more concretely.

CONCLUSION

The lacustrine carbonate isotope record for CV reveals a rich continuous history of hydroclimate spanning the last ~2.9 million years. We argue that although the lake sustains high overall isotope values due to evaporative enrichment, million-year scale variations are driven by changes in the seasonality of precipitation being transported to the basin as well as changes in P-E. Specifically, we argue that the late Pliocene to early Pleistocene saw enhanced convergent monsoonal circulation, and through the middle to late Pleistocene, strengthened southwesterly moisture delivery could have resulted in greater wintertime precipitation. We find a covariance between carbonate oxygen isotopes and paired bulk lithium concentrations, which we attribute to the effects of evapoconcentration prior to authigenic clay precipitation in the lake water. This

finding suggests that climate may play a key role in the concentration of lithium in authigenic lacustrine clays in terminal basins containing pluvial lake systems.

ACKNOWLEDGEMENTS

This work was partially supported by NSF/GSA Graduate Student Geoscience Grant # 13087-21 to CAG, which is funded by NSF Award # 1949901, and funding from the Miller Institute at UC Berkeley to DEI. TB was supported by NSF P2C2 Grant OCE-1903148. DEI and CG were partially supported by P2C2 Grant AGS-2102901. We greatly appreciate the Albermarle Corporation for providing access to CV drill cores. We would like to thank Steven Clemens for assistance with the carbonate stable isotope measurements; Hari Mix and Michele Bezanson for help with fieldwork; and Sylvia Dee and Jim Russell for lake discussions and assistance with HYSPLIT analyses.

REFERENCES

Annan, J. D., & Hargreaves, J. C., 2013, A new global reconstruction of temperature changes at the Last Glacial Maximum: *Climate of the Past*, v. *9*, p. 367-376.

Araoka, D., Kawahata, H., Takagi, T., Watanabe, Y., Nishimura, K., & Nishio, Y., 2014, Lithium and strontium isotopic systematics in playas in Nevada, USA: constraints on the origin of lithium: *Mineralium Deposita*, v. *49*, p. 371-379.

Bhattacharya, T., Tierney, J. E., & DiNezio, P., 2017, Glacial reduction of the North American Monsoon via surface cooling and atmospheric ventilation: *Geophysical Research Letters*, v. *44*, p. 5113-5122.

Blaauw, M., & Christen, J. A., 2011, Flexible paleoclimate age-depth models using an autoregressive gamma process: *Bayesian analysis*, *6*(3), 457-474.

Bowen, G. J., 2022, The Online Isotopes in Precipitation Calculator, version 3.1. http://www.waterisotopes.org.

Bowen G. J. and Revenaugh J. , 2003, Interpolating the isotopic composition of modern meteoric precipitation: *Water Resources Research* 39(10), 1299, doi:10.129/2003WR002086.

Bradley, D. C., Munk, L., Jochens, H., Hynek, S., & Labay, K., 2013, *A preliminary deposit model for lithium brines*: US Department of the Interior, US Geological Survey.

Brooks, L. E., Masbruch, M. D., Sweetkind, D. S., & Buto, S. G., 2014, Steady-state numerical groundwater flow model of the Great Basin carbonate and alluvial aquifer system: *US Geological Survey Scientific Investigation Report*, 124.

Burke, K. D., Williams, J. W., Chandler, M. A., Haywood, A. M., Lunt, D. J., & Otto-Bliesner, B. L., 2018, Pliocene and Eocene provide best analogs for near-future climates: *Proceedings of the National Academy of Sciences*, v. *115*, p. 13288-13293.

Burls, N. J., & Fedorov, A. V.,2017, Wetter subtropics in a warmer world: Contrasting past and future hydrological cycles: *Proceedings of the National Academy of Sciences*, v. *114*, p. 12888-12893.

Burrus, J. B., 2013, Structural and stratigraphic evolution of the Weepah Hills Area, NV: transition from basin-and-range extension to Miocene core complex formation[Master's Thesis]: University of Texas at Austin.

Calvo, J. P., Blanc-Valleron, M. M., Rodrígues-Arandía, J. P., Rouchy, J. M., & Sanz, M. E. (1999). Authigenic clay minerals in continental evaporitic environments. Special

572 Publications of the International Association of Sedimentologists, 27, 129–151.
573 https://doi.org/10.1002/9781444304190
574 Carroll, A. R., & Bohacs, K. M.,1999, Stratigraphic classification of ancient lakes: Balancing
575 tectonic and climatic controls: *Geology*, v. *27*, p. 99-102.
576 Castor, S. B., & Henry, C. D., 2020, Lithium-rich claystone in the McDermitt Caldera, Nevada,
577 USA: Geologic, mineralogical, and geochemical characteristics and possible origin:
578 *Minerals*, v. *10*, p. 68.
579 Caves, Jeremy K., A. J. Ritch, D. E. Ibarra, C. P. Chamberlain, B. U. Bayshashov, A.
580 Zhamangara, D. J. Sjostrom, H. T. Mix, & M. J. Winnick, 2017, Late Miocene uplift of
581 the Tian Shan and Altai and reorganization of Central Asia climate: *GSA Today, 27*(2),
582 20-26.
583 Clark, P. U., Dyke, A. S., Shakun, J. D., Carlson, A. E., Clark, J., Wohlfarth, B., Mitrovica, J.X.,
584 Hostetler, S. W., McCabe, A. M.,2009, The last glacial maximum: *Science*, v. *325*, p.
585 710-714.
586 Coffey, D. M., Munk, L. A., Ibarra, D. E., Butler, K. L., Boutt, D. F., & Jenckes, J., 2021,
587 Lithium Storage and Release from Lacustrine Sediments: Implications for Lithium
588 Enrichment and Sustainability in Continental Brines: *Geochemistry, Geophysics,*
589 *Geosystems*, v. 22, p. e2021GC009916.
590 Davis, J. R. (1981). Late Cenozoic geology of Clayton Valley, Nevada and the genesis of a
591 lithium-enriched brine (Ph.D. Dissertation, p. 283). University of Texas Austin.
592 Davis, J. R., Friedman, I., & Gleason, J. D., 1986, Origin of the lithium-rich brine, Clayton
593 Valley, Nevada: *US Geological Survey Bulletin*, v. *1622*, p. 131-138.

De Masi, C. L., 2013, *Ancient sedimentary fill of the Waucobi Lake Beds as an archive of Owens Valley, California tectonics and climate*. California State University, Long Beach.

Dowsett, H. J., & Caballero Gill, R. P., 2010, Pliocene climate: *Stratigraphy*, v. *7*, p. 106-110.

Forester, R. M., Lowenstein, T. K., & Spencer, R. J., 2005, An ostracode based paleolimnologic and paleohydrologic history of Death Valley: 200 to 0 ka: *Geological Society of America Bulletin*, v. *117*, p. 1379-1386.

Fu, M., Cane, M. A., Molnar, P., & Tziperman, E., 2022, Warmer Pliocene upwelling site SST leads to wetter subtropical coastal areas: a positive feedback on SST: *Paleoceanography and Paleoclimatology*, v. 37, p. e2021PA004357.

Godsey, H. S., Oviatt, C. G., Miller, D. M., & Chan, M. A., 2011, Stratigraphy and chronology of offshore to nearshore deposits associated with the Provo shoreline, Pleistocene Lake Bonneville, Utah: *Palaeogeography, Palaeoclimatology, Palaeoecology*, v. *310*, p. 442-450.

A.M. Haywood, J.C. Tindall, H.J. Dowsett, A.M. Dolan, K.M. Foley, S.J. Hunter, D.J. Hill, W.L. Chan, A. Abe-Ouchi, C. Stepanek, G. Lohmann, D. Chandan, W.R. Peltier, N. Tan, C. Contoux, G. Ramstein, X. Li, Z. Zhang, C. Guo, K.H. Nisancioglu, Q. Zhang, Q. Li, Y. Kamae, M.A. Chandler, L.E. Sohl, B.L. Otto-Bliesner, R. Feng, E.C. Brady, A.S. von der Heydt, M.L.J. Baatsen, D.J. Lunt, 2020, The Pliocene Model Intercomparison Project Phase 2: large-scale climate features and climate sensitivity: *Climate of the Past*, v. *16*, p. 2095-2123.

Hildreth, W., Fierstein, J., Phillips, F. M., & Calvert, A., 2021, Trachyandesite of Kennedy Table, its vent complex, and post− 9.3 Ma uplift of the central Sierra Nevada: *GSA Bulletin*.

617 Ibarra, D. E., Egger, A. E., Weaver, K. L., Harris, C. R., & Maher, K., 2014, Rise and fall of late
618 Pleistocene pluvial lakes in response to reduced evaporation and precipitation: Evidence
619 from Lake Surprise, California: *GSA Bulletin*, v. 126, p. 1387-1415.
620 Ibarra, D. E., Oster, J. L., Winnick, M. J., Caves Rugenstein, J. K., Byrne, M. P., & Chamberlain,
621 C. P., 2018, Warm and cold wet states in the western United States during the Pliocene–
622 Pleistocene. *Geology*, v. *46*, p. 355-358.
623 Ingersoll, R. V., 2019, Subduction-Related Sedimentary Basins of the US Cordillera, *in* The
624 Sedimentary Basins of the United States and Canada, Elsevier, p. 477-510.
625 Jannik, N. O., Phillips, F. M., Smith, G. I., & Elmore, D., 1991, A 36Cl chronology of lacustrine
626 sedimentation in the Pleistocene Owens River system: *GSA Bulletin*, v. *103*, p. 1146-
627 1159.
628 Kim, S. T., & O'Neil, J. R., 1997, Equilibrium and nonequilibrium oxygen isotope effects in
629 synthetic carbonates: *Geochimica et cosmochimica acta*, v. *61*, p. 3461-3475.
630 Kloprogge, J. T., Komarneni, S., & Amonette, J. E. (1999). Synthesis of smectite clay minerals:
631 A critical review. Clays and Clay Minerals, 47(5), 529–554.
632 https://doi.org/10.1346/ccmn.1999.0470
633 Knott, J. R., Machette, M. N., Wan, E., Klinger, R. E., Liddicoat, J. C., Sarna-Wojcicki, A. M.,
634 Fleck, R. J., Deino, A. L., Geissman, J. W., Slate J. L., Wahl D. B., Wernicke, B. P.,
635 Wells, S. G., Tinsley III, Hathaway, J. C., Weamer, V. M., 2018, Late Neogene–
636 Quaternary tephrochronology, stratigraphy, and paleoclimate of Death Valley, California,
637 USA: *GSA Bulletin*, v. *130*, p. 1231-1255.
638 Knott, J. R., Wan, E., Deino, A. L., Casteel, M., Reheis, M. C., Phillips, F. M., Walkup, L.,
639 McCarty, K., Manoukian, D. N., Nunez, E., 2019, Lake Andrei: A pliocene pluvial lake

in Eureka Valley, eastern California: *From Saline to Freshwater: The Diversity of Western Lakes in Space and Time, S. Starratt and MR Rosen, Eds, 536*, 125-142.

Kunasz, I. A., 1974, Lithium occurrence in the brines of Clayton Valley, Esmeralda County, Nevada. In Fourth Symposium on Salt–Northern Ohio Geological Survey (pp. 57-66).

Kurth, G., Phillips, F. M., Reheis, M. C., Redwine, J. L., & Paces, J. B., 2011, Cosmogenic nuclide and uranium-series dating of old, high shorelines in the western Great Basin, USA: *GSA Bulletin*, v. *123*, p. 744-768.

Lee, J.-Y., J. Marotzke, G. Bala, L. Cao, S. Corti, J.P. Dunne, F. Engelbrecht, E. Fischer, J.C. Fyfe, C. Jones, A. Maycock, J. Mutemi, O. Ndiaye, S. Panickal, and T. Zhou, 2021, Future Global Climate: Scenario-Based Projections and Near-Term Information. In Climate Change 2021: The Physical Science Basis. Contribution of Working Group I to the Sixth Assessment Report of the Intergovernmental Panel on Climate Change [Masson-Delmotte, V., P. Zhai, A. Pirani, S.L. Connors, C. Péan, S. Berger, N. Caud, Y. Chen, L. Goldfarb, M.I. Gomis, M. Huang, K. Leitzell, E. Lonnoy, J.B.R. Matthews, T.K. Maycock, T. Waterfield, O. Yelekçi, R. Yu, and B. Zhou (eds.)]. Cambridge University Press. In Press.

Leng, M. J., & Marshall, J. D., 2004, Palaeoclimate interpretation of stable isotope data from lake sediment archives: *Quaternary Science Reviews*, v. *23*, p. 811-831.

Li, C., Li, Z., Wu, T., Luo, Y., Zhao, J., Li, X., Yang, W. & Chen, X., 2021, Metallogenic characteristics and formation mechanism of Naomugeng clay-type lithium deposit in central inner Mongolia, China: *Minerals*, 11(3), 238.

Li, H. C., & Ku, T. L., 1997, δ13C–δ18C covariance as a paleohydrological indicator for closed-basin lakes: *Palaeogeography, Palaeoclimatology, Palaeoecology*, v. *133*, p. 69-80.

663 Lora, J. M., & Ibarra, D. E., 2019, The North American hydrologic cycle through the last
664 deglaciation: *Quaternary Science Reviews*, v. *226*, p. 105991.
665 Loveday, Derek & Turner, Al., 2020, NI43-101 American Lithium TLC Lithium Property,
666 Nevada, USA.
667 Lowenstein, T. K., Li, J., Brown, C., Roberts, S. M., Ku, T. L., Luo, S., & Yang, W., 1999, 200
668 ky paleoclimate record from Death Valley salt core: *Geology*, v. *27*, p. 3-6.
669 Manthiram, A., 2017, An outlook on lithium ion battery technology. *ACS central science*, v.
670 3(10), p. 1063-1069.
671 Matsubara, Y., and Howard, A.D., 2009, A spatially explicit model of runoff, evaporation, and
672 lake extent: Application to modern and late Pleistocene lakes in the Great Basin region,
673 western United States: *Water Resources Research*, v. 45.
674 Means, J.D., 2013, GPS precipitable water as a diagnostic of the North American monsoon in
675 California and Nevada: *Journal of Climate*, v. *26*, p. 1432-1444.
676 Mifflin M.D. Wheat M.M., 1979, Pluvial Lakes and Estimated Pluvial Climates of Nevada:
677 Nevada Bureau of Mines and Geology Bulletin, v. 94, 57 p.
678 Mix, H. T., Rugenstein, J. K. C., Reilly, S. P., Ritch, A. J., Winnick, M. J., Kukla, T., &
679 Chamberlain, C. P., 2019, Atmospheric flow deflection in the late Cenozoic Sierra
680 Nevada: *Earth and Planetary Science Letters*, v. *518*, p. 76-85.
681 Molnar, P., & Cane, M. A., 2002, El Niño's tropical climate and teleconnections as a blueprint
682 for pre-Ice Age climates: *Paleoceanography*, 17(2), 11-1.
683 Morissette, C. L., 2012, The impact of geological environment on the lithium concentration and
684 structural composition of hectorite clays. University of Nevada, Reno.

685 Munk, L., & Chamberlain, C. P., 2011, Final Technical Report: G10AP00056-Lithium Brine
686 Resources: A Predictive Exploration Model. *Research supported by the US Geological*
687 *Survey (USGS), Department of the Interior, under USGS award*, (G10AP00056).
688 Munk, L., Jennings, M., Bradley, D., Hynek, S., Godfrey, L., & Jochens, H. (2011, September).
689 Geochemistry of lithium-rich brines in Clayton Valley, Nevada, USA. In *Proceedings of*
690 *the 11th SGA Biennial Meeting, Antofagasta, Chile* (pp. 26-29).
691 Munk, L. A., Hynek, S. A., Bradley, D., Boutt, D., Labay, K., & Jochens, H., 2016, Lithum
692 brines: A global perspective: *Reviews in Economic Geology*, v. 18, p. 339-365.
693 Munroe, J. S., & Laabs, B. J., 2013, Latest Pleistocene history of pluvial Lake Franklin,
694 northeastern Nevada, USA: *GSA Bulletin*, v. *125*, p. 322-342.
695 Oldow, J. S., Elias, E. A., Ferranti, L., McClelland, W. C., McIntosh, W. C., & Cashman, P. H.,
696 2009, Late Miocene to Pliocene synextensional deposition in fault-bounded basins within
697 the upper plate of the western Silver Peak–Lone Mountain extensional complex, west-
698 central Nevada: *Late Cenozoic Structure and Evolution of the Great Basin–Sierra*
699 *Nevada Transition: Geological Society of America Special Paper*, *447*, 275-312.
700 Orme, A. R., 2008, Pleistocene pluvial lakes of the American West: a short history of research:
701 *Geological Society, London, Special Publications*, v. *301*, p. 51-78.
702 Oster, J. L., & Ibarra, D. E., 2018, Glacial hydroclimate of western North America: insights from
703 proxy-model comparison and implications for Lake Bonneville, *Utah Geological Survey*
704 *Miscellaneous Publications*, v. 170, p. 8.
705 Oster, J. L., Weisman, I. E., & Sharp, W. D., 2020, Multi-proxy stalagmite records from northern
706 California reveal dynamic patterns of regional hydroclimate over the last glacial cycle:
707 *Quaternary Science Reviews*, v. *241*, p. 106411.

Pound, M. J., Tindall, J., Pickering, S. J., Haywood, A. M., Dowsett, H. J., & Salzmann, U., 2014, Late Pliocene lakes and soils: a global data set for the analysis of climate feedbacks in a warmer world: *Climate of the Past*, v. *10*, p. 167-180.

Ravelo, A. C., Andreasen, D. H., Lyle, M., Olivarez Lyle, A., & Wara, M. W., 2004, Regional climate shifts caused by gradual global cooling in the Pliocene epoch: *Nature*, v. *429*, p. 263-267.

Ray, A. J., Garfin, G. M., Wilder, M., Vásquez-León, M., Lenart, M., & Comrie, A. C., 2007, Applications of monsoon research: Opportunities to inform decision making and reduce regional vulnerability: *Journal of Climate*, v. *20*, p. 1608-1627.

Reheis, M.C., 1991, Geologic map of late Cenozoic deposits and faults in the western part of the Rhyolite Ridge 15-minute quadrangle, Esmeralda County, Nevada: U.S. Geological Survey Miscellaneous Investigations Series Map I–2183, scale 1:24,000.

Reheis, M.C., 1992, Geologic map of Late Cenozoic deposits and faults in parts of the Soldier Pass and Magruder Mountain 15-minute quadrangles, Inyo and Mono Counties, California, and Esmeralda County, Nevada: U.S. Geological Survey Miscellaneous Investigations Series Map I–2268, scale 1:24,000

Reheis, M. C., Slate, J. L., Sarna-Wojcicki, A. M., & Meyer, C. E.,1993, A late Pliocene to middle Pleistocene pluvial lake in Fish Lake Valley, Nevada and California: *Geological Society of America Bulletin*, v. *105*, p. 953-967.

Reheis, M.,1999, Highest pluvial-lake shorelines and Pleistocene climate of the western Great Basin: *Quaternary research*, v. *52*, p. 196-205.

Reheis M.C.,1999a, Extent of Pleistocene Lakes in the Western Great Basin: U.S. Geological Survey Miscellaneous Field Studies Map MF-2323, scale 1:800, 000, 1 sheet.

731 Reheis, M. C., A. M. Sarna-Wojcicki, R. L. Reynolds, C. A. Repenning, and M. D. Mifflen,
732 2002, Pliocene to middle Pleistocene lakes in the western Great Basin: Ages and
733 connections, in Great Basin Aquatic Systems History, edited by R. Hershler, D. Currey,
734 and D. Madsen, Smithson. Contrib. Earth Sci., v. 33, p. 53–108.
735 Reheis, M. C., & Block, D. L., 2007, Surficial Geologic Map and Geochronologic Database, Fish
736 Lake Valley, Esmeralda County, Nevada, and Mono County, California (No. 277).
737 Geological Survey (US).
738 Reheis, M. C., Adams, K. D., Oviatt, C. G., & Bacon, S. N., 2014, Pluvial lakes in the Great
739 Basin of the western United States—a view from the outcrop: *Quaternary Science*
740 *Reviews*, v. *97*, p. 33-57.
741 Robinson, G. D., Klepper, M. R., & Obradovich, J. D., 1968, Overlapping plutonism, volcanism,
742 and tectonism in the Boulder batholith region, western Montana: GSA Memoir 116.
743 Rowley, D.B., and Currie, B.S., 2006, Palaeoaltimetry of the late Eocene to Miocene Lunpola
744 basin, central Tibet: Nature, v. 439, p. 677–681,
745 doi: 10.1038/nature04506
746 Rush, F. E.,1968, *Water-resources Appraisal of Clayton Valley-Stonewall Flat Area, Nevada*
747 *and California*. State of Nevada, Department of Conservation and Natural Resources.
748 Salzmann, U., Williams, M., Haywood, A. M., Johnson, A. L., Kender, S., & Zalasiewicz, J.,
749 2011, Climate and environment of a Pliocene warm world: *Palaeogeography,*
750 *Palaeoclimatology*, *Palaeoecology*, v. *309*, p. 1-8.
751 Santi, L. M., Arnold, A. J., Ibarra, D. E., Whicker, C. A., Mering, J. A., Lomarda, R. B., Lora, J.
752 M., Tripati, A., 2020, Clumped isotope constraints on changes in latest Pleistocene

753 hydroclimate in the northwestern Great Basin: Lake Surprise, California: *GSA Bulletin*, v.
754 *132*, p. 2669-2683.
755 Sarna-Wojcicki, A.M., Reheis, M.C., Pringle, M.S., Fleck, R.J., Burbank, Doug, Meyer, C.E.,
756 Slate, J.L., Wan, Elmira, Budahn, J.R., Troxel, Bennie, and Walker, J.P., 2005, Tephra
757 layers of Blind Spring Valley and related upper Pliocene and Pleistocene tephra layers,
758 California, Nevada, and Utah—Isotopic ages, correlation, and magnetostratigraphy: U.S.
759 Geological Survey Professional Paper 1701, 63 p.
760 Smith, G. I.,1983, Core KM-3, a surface-to-bedrock record of late Cenozoic sedimentation in
761 Searles Valley, California.
762 Smith, G.I., Bishchoff, J.L., and Bradbury, J.P., 1997, Synthesis of the paleoclimatic record from
763 Owens Lake core OL-92, in Smith, G.I., and Bishchoff, J.L.,eds., An 800,000-Year
764 Paleoclimatic Record from Core OL-92: Geological Society of America Special Paper
765 317,p. 143–160.
766 Starkey, H. C. (1982). The role of clays in fixing lithium (p. 8). U.S. Geological Survey Bulletin
767 1278-F. Retrieved from https://pubs.usgs.gov/bul/1278f/report.pd
768 Stein, A. F., Draxler, R. R., Rolph, G. D., Stunder, B. J., Cohen, M. D., & Ngan, F., 2015,
769 NOAA's HYSPLIT atmospheric transport and dispersion modeling system: *Bulletin of*
770 *the American Meteorological Society*, v. *96*, p. 2059-2077.
771 Sweetkind, D. S., Masbrunch, M. D., Heilweil, V. M., & Buto, S. G. (2010). Chapter C:
772 Groundwater flow. In V. M. Heilweil, & L. E. Brooks (Eds.), Conceptual model of the
773 Great Basin carbonate and alluvial aquifer system (p. 191). U.S. Geological Survey
774 Scientific Investigations Report 2010-5193.

Teng, F. Z., McDonough, W. F., Rudnick, R. L., Dalpé, C., Tomascak, P. B., Chappell, B. W., & Gao, S., 2004, Lithium isotopic composition and concentration of the upper continental crust: *Geochimica et Cosmochimica Acta*, v. *68*, p. 4167-4178.

Underdown, C. G., Boutt, D. F., Hynek, S. A., & Munk, L. A., 2017, Evaluating Hydrologic Transience in Watershed Delineation, Numerical Modeling and Solute Transport in the Great Basin. Clayton Valley, Nevada: *AGU Fall Meeting Abstracts*, v. 2017, p. H53O-08).

Warner, M. S., 2018, Introduction to PySPLIT: A Python toolkit for NOAA ARL's HYSPLIT model: *Computing in Science & Engineering*, v. *20*, p. 47-62.

Welker, J. M.,2012, ENSO effects on δ18O, δ2H and d-excess values in precipitation across the US using a high-density, long-term network (USNIP): *Rapid Communications in Mass Spectrometry*, v. *26*, p. 1893-1898.

Welker J.M., 2000, Isotopic (d18O) characteristics of weekly precipitation collected across the USA: An initial analysis with application to water source studies: *Hydrological Processes* 14, 1449-1464.

FIGURES

Fig 1. Regional Map of Study Site

Fig 2. EXP2 Age Model

Fig 3. Geochronology results

Fig 4. Thin Sections

Fig 5. CV Stable Isotope record

Fig 6. HYSPLIT seasonality

798 **Fig 7.** HYSPLIT paired isotope seasonality

799 **Fig 8.** Fish Lake Valley isotope record

800 **Fig 9.** Lithium-$\delta^{18}O$ cross plot

801

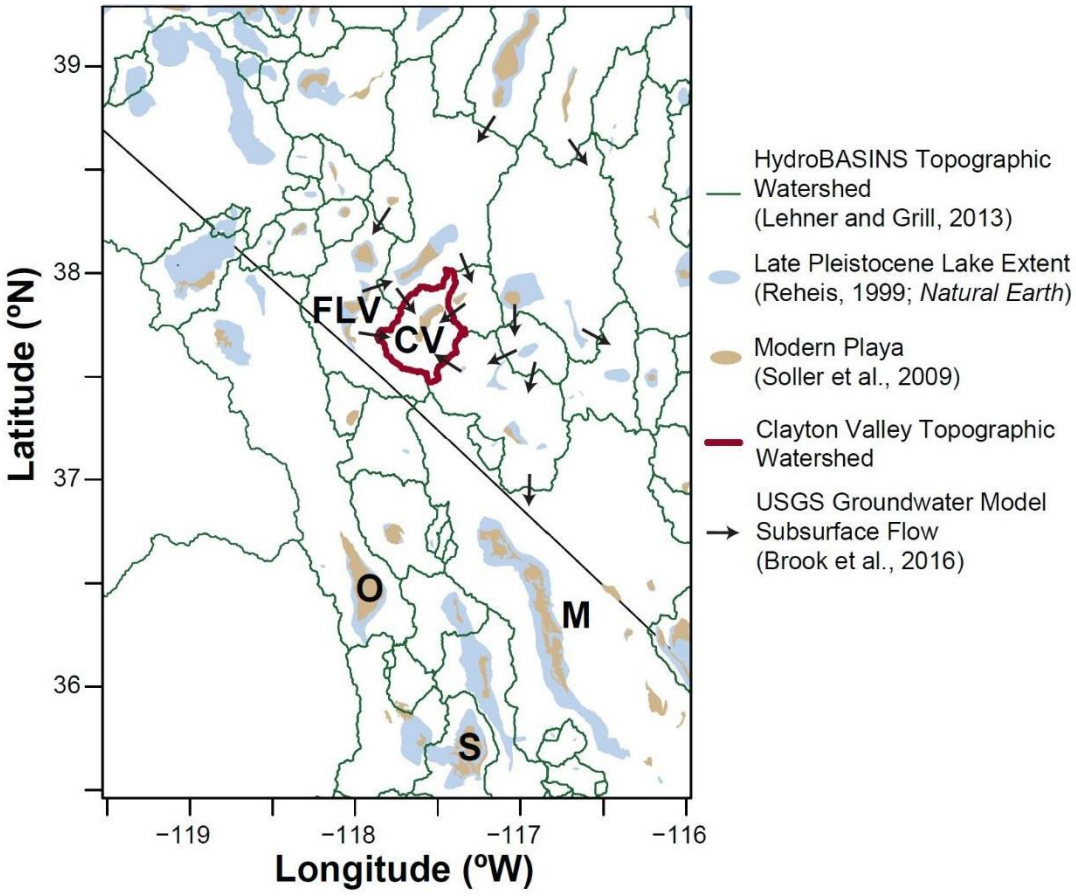

802

803 **Fig 1.** Map of Clayton Valley (CV), Fish Lake Valley (FLV), Lake Manly (M), Searles Lake (S),

804 and Owens Valley (O) with watershed boundaries, late Pleistocene lake extents and modern

805 playas. Note that the groundwater flow vectors (Brook et al., 2016) surrounding the study site

806 terminate in the CV basin.

807

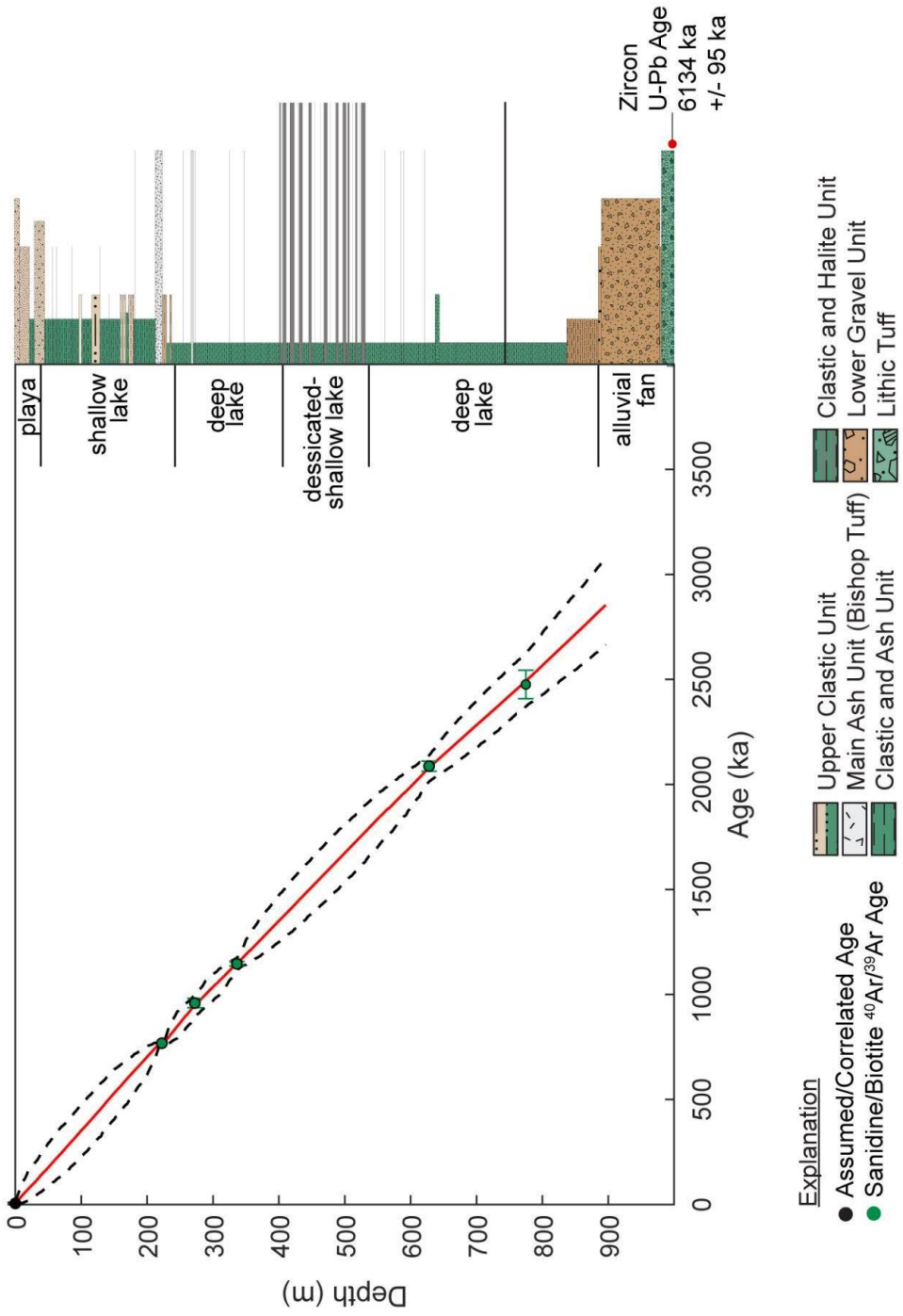

Fig 2. Age model for Clayton Valley EXP2 core alongside a stratigraphic column detailing the major lithologic units modified from Coffey et al. (2021). Light gray units in the stratigraphic column are halite beds, while thin black units are ashes.

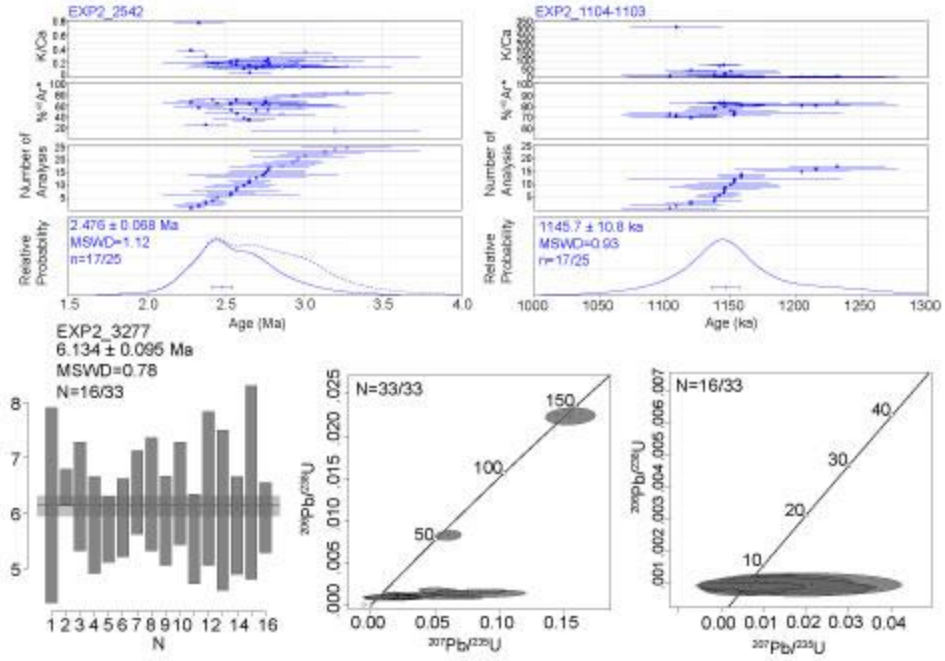

812

813 **Fig 3.** Age calculation from volcanic ashes. From top right to bottom left: 40Ar-39Ar results for
814 samples EXP2_1104-1103 and EXP2_2542 showing KCa, %40Ar, number of analysis, and
815 relative probability by age, including which analyses were used in the age calculation; and U-Pb
816 results shown as concordia plots and weight mean average age calculation for sample
817 EXP2_3277.

818

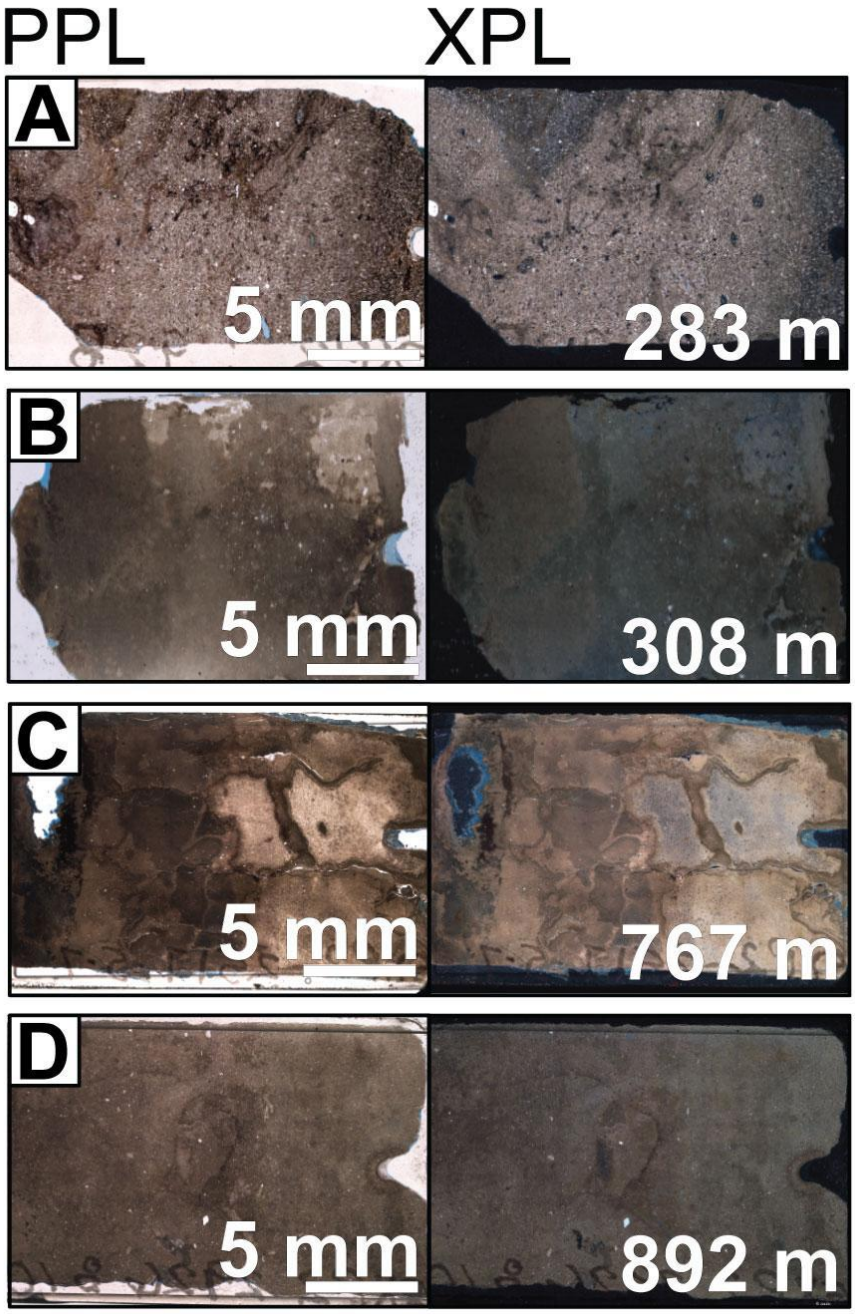

819

820 **Fig 4.** Photomicrogaphs of select lacustrine carbonate intervals from the EXP2 core in plane
821 polarized light (PPL) and cross-polarized light (XPL) showing rare mixed clastic-carbonate
822 intervals (A,D) and micritic text with limited porosity (B-D). Scale bar (5 mm) is displayed on
823 PPL image and core depth in meters is displayed on XPL image.

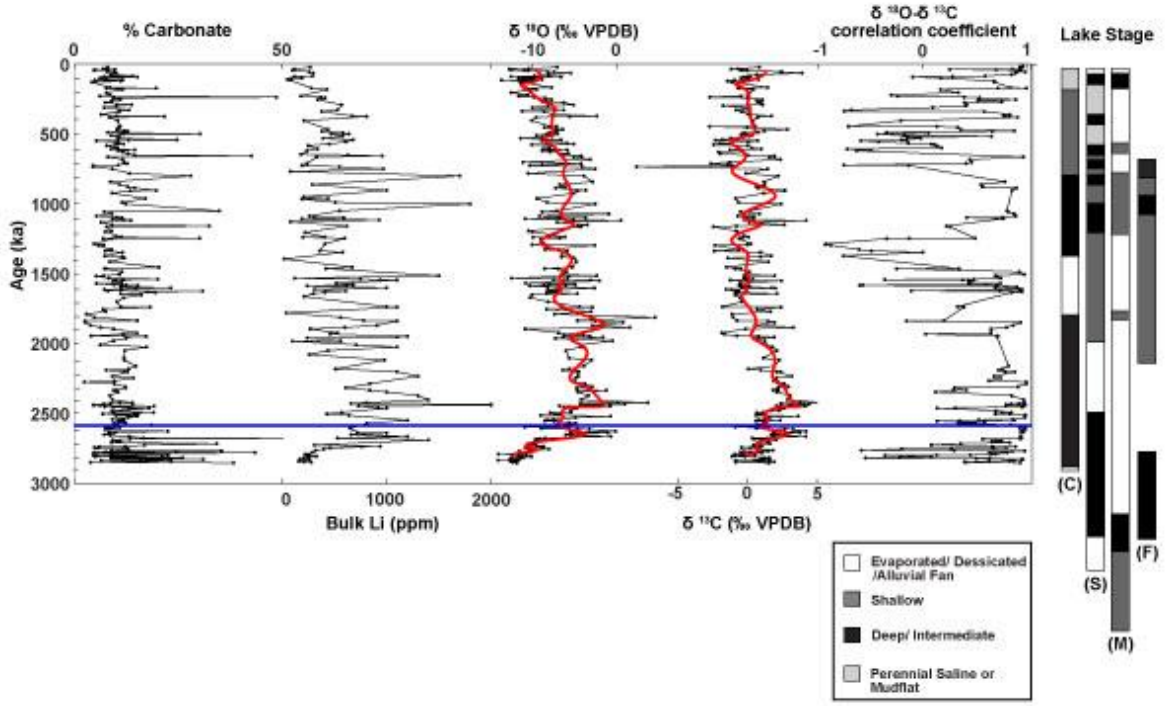

824

825 **Fig 5.** Time series from the Clayton Valley EXP2 core. From left to right: percent carbonate;
826 bulk sediment lithium concentrations (ppm); carbonate $\delta^{18}O$ (‰, VPDB); carbonate $\delta^{13}C$ (‰,
827 VPDB); running correlation coefficient between oxygen and carbon isotopes with a moving
828 window of 10 data points; lake stage for Clayton Valley compared to neighboring valleys
829 adapted after Knott et al. (2019) were (C) is Clayton Valley, (S) is Searles Lake, (M) is Lake
830 Manly, and (F) is Fish Lake Valley. Solid red lines are a low pass filtered curve on the carbonate
831 $\delta^{18}O$ and $\delta^{13}C$ records. Blue horizontal line marks the Pliocene-Pleistocene boundary (2588 ka).

832

833

834

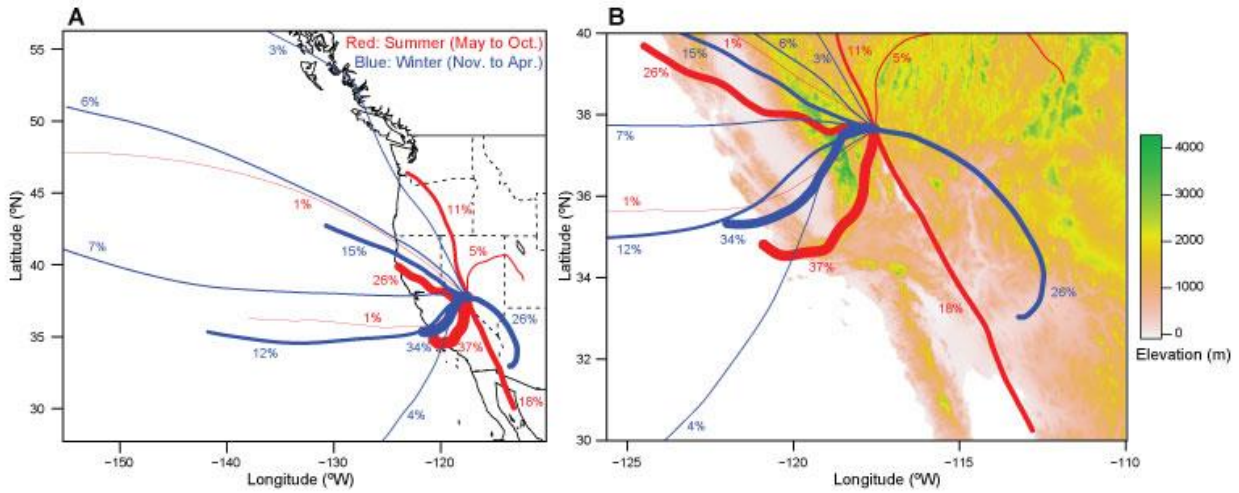

835

836 **Fig 6.** (A) Average winter (blue) and summer (red) 3-day air mass back trajectories for CV

837 weighted by precipitation; (B) same as left panel but zoomed in with elevation contoured.

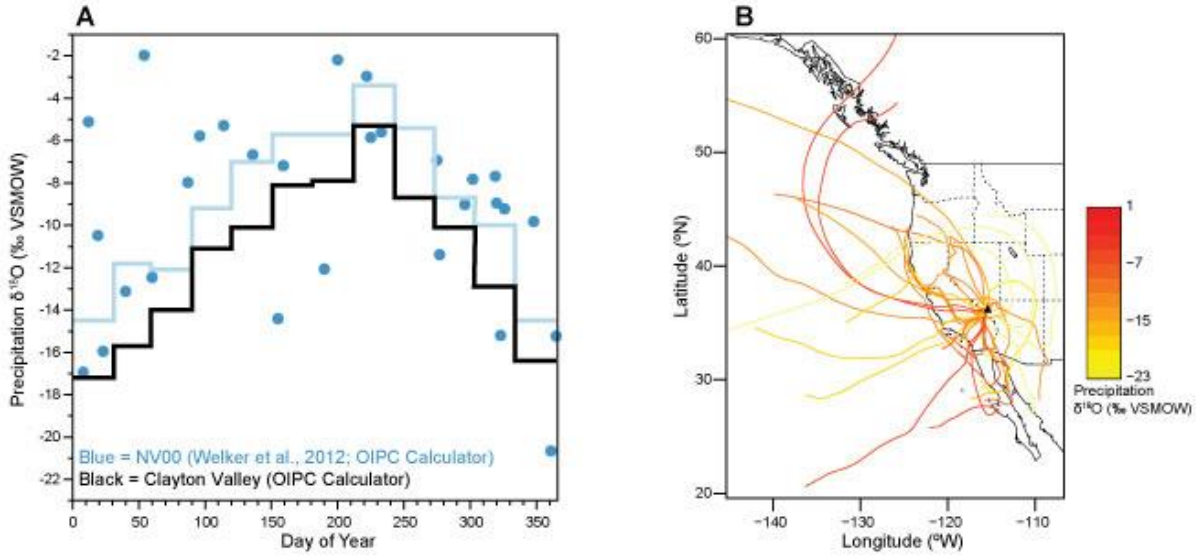

838

839

840 **Fig 7.** (A) Measured (dots) versus calculated (solid lines) precipitation $\delta^{18}O$ (VSMOW)

841 throughout the year for CV (Black) and Las Vegas, NV (light blue). Calculations were made

842 using the Oxygen Isotope Precipitation Calculator (OIPC; Welker, 2000; Bowen and Revenaugh,

843 2003; Bowen, 2022). (B) Annual average 3-day air mass back trajectories for Las Vegas

844 weighted by precipitation. Colors indicate modern precipitation isotope values (Welker, 2012)

845 recorded in Las Vegas, NV.

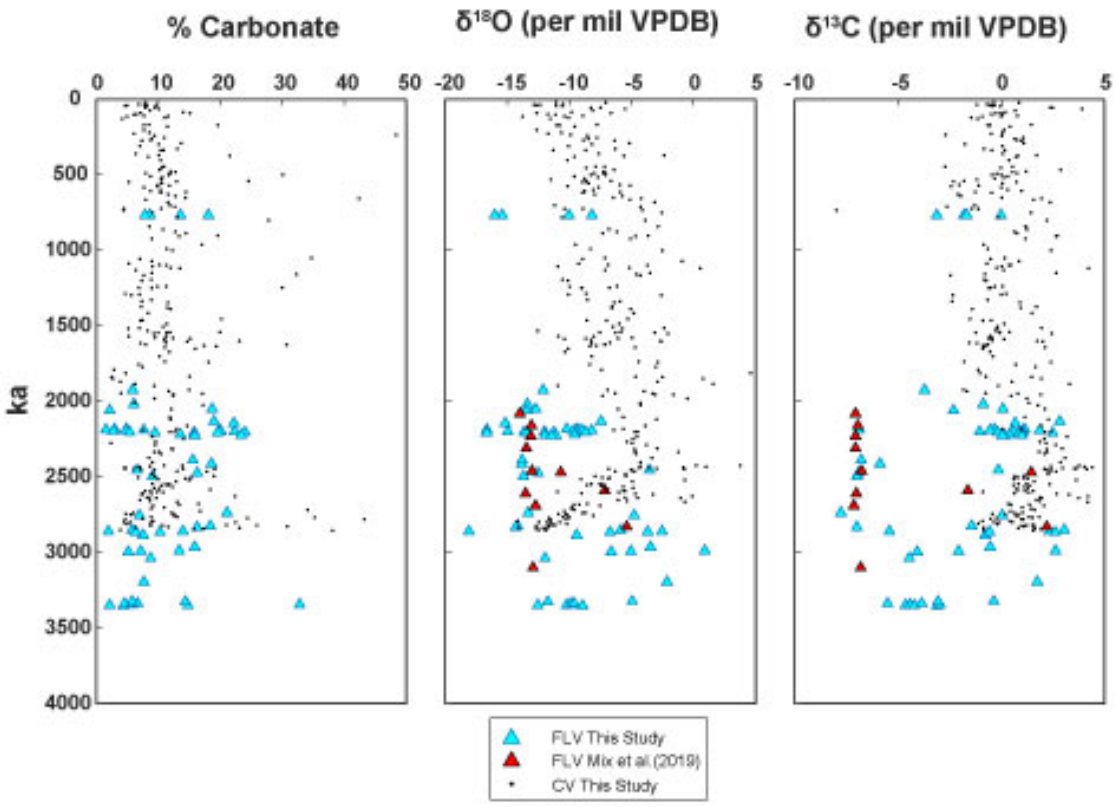

846

847 **Fig 8.** Stable isotopes of Clayton Valley carbonates compared to neighboring Fish Lake Valley

848 (FLV). FLV samples from this study (in blue) were collected in the summer of 2021. Red

849 samples are taken from Mix et al. (2019). Shown in black are values for Clayton Valley.

850

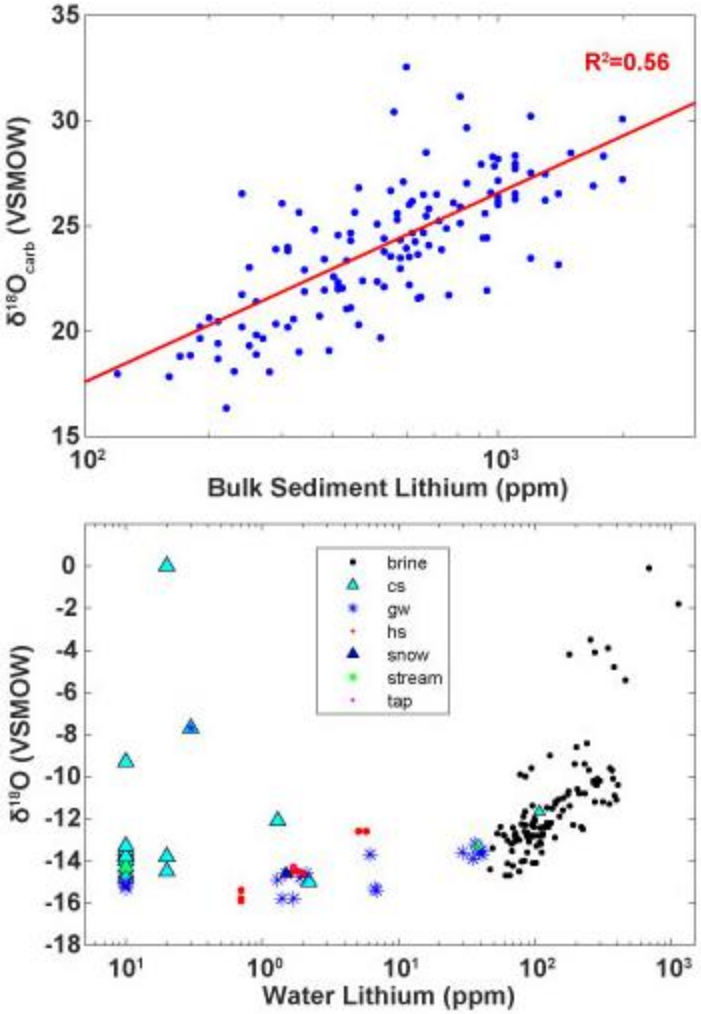

851

852 **Fig 9.** (A) Bulk sediment lithium concentrations (ppm) for EXP2 samples paired with carbonate
853 oxygen isotope values (per mil VSMOW). The red line is a logarithmic fit with an R^2 value of
854 0.56. (B) Lithium (ppm) and oxygen isotope values (per mil VSMOW) of natural water samples
855 taken around Clayton Valley. "Cs" refers to cold spring water samples, "hs" stands for hot spring
856 water, and "gw" stands for groundwater.

SUPPLEMENTARY MATERIALS

for

Paleoclimate controls on lithium enrichment in Great Basin Pliocene-Pleistocene lacustrine clays

Catherine A. Gagnon[1,2,†], Kristina L. Butler[3], Elizabeth Gaviria[1,4], Alexa Terrazas[5], Annabelle Gao[1], Tripti Bhattacharya[6], David F. Boutt[7], Lee Ann Munk[8], Daniel E. Ibarra[1,2]

[1]*Department of Earth, Environmental and Planetary Science, Brown University, Providence, RI 02912, USA*

[2]*Institute at Brown for Environment and Society, Brown University, Providence, RI 02912, USA*

[3]*Department of Geological Sciences, Jackson School of Geosciences, University of Texas at Austin, Austin, TX 78712, USA*

[4]*Department of Earth, Environmental and Planetary Sciences, Rice University, Houston, TX 77005, USA*

[5]*Department of Ocean and Atmospheric Sciences, University of California, Los Angeles, CA, 90095, USA*

[6]*Department of Earth Sciences, Syracuse University, Syracuse, NY 12344, USA*

[7]*Department of Geosciences, University of Massachusetts-Amherst, Amherst, MA 01003, USA*

[8]*Department of Geological Sciences, University of Alaska Anchorage, Anchorage, AK 99508, USA*

† Corresponding author: catherine_gagnon@brown.edu

The following is included in this file:

Figure S1. Age Model with Halite Slumps

Figure S2. EXP2 Time series with weathering indices

Figures S3. CIA ternary diagram

The following is included in an attached Excel File:

Table S1. EXP2 age constraints

Table S2. EXP2 samples and data table

Table S3. Zircon U-Pb data

Table S4. 40Ar/39Ar data

Table S5. Fish Lake Valley age constraints

Table S6. Fish Lake Valley samples and data table

Table S7. Modern water samples

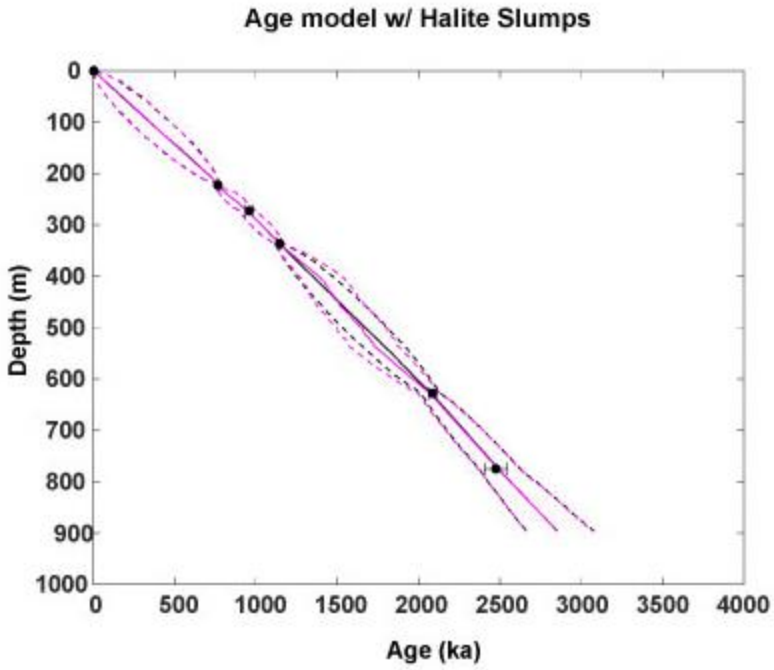

Fig S1. Bacon age-depth model using ash slumps only (black) and added halite slumps (magenta). Age control points are the same as Fig 1.

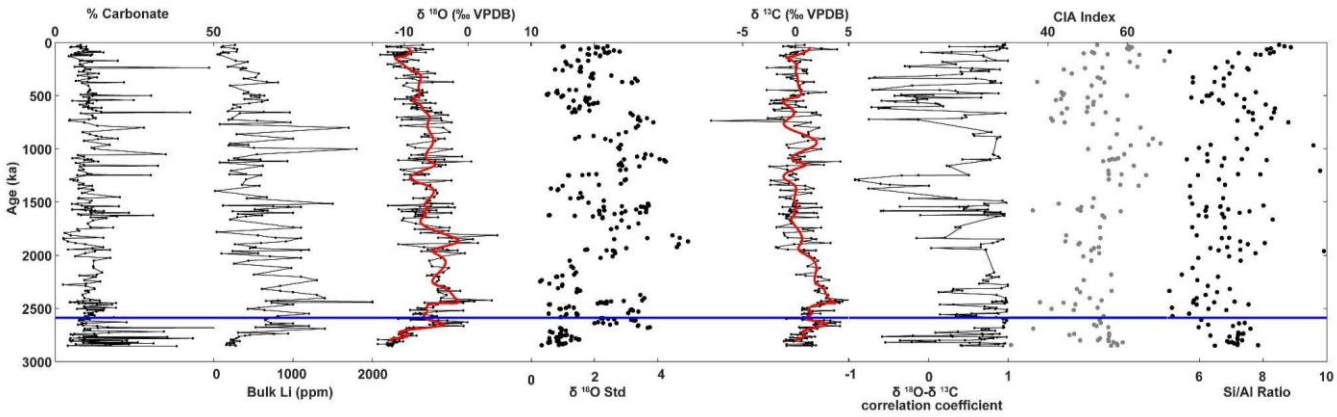

Figure S2. Full time series from the Clayton Valley EXP2. From left to right: percent carbonate; bulk sediment lithium concentrations (ppm); carbonate $\delta^{18}O$ (‰ VPDB); 5 point running carbonate $\delta^{18}O$ standard deviation; carbonate $\delta^{13}C$ (‰ VPDB); correlation coefficient between oxygen and carbon isotopes with a moving window of 10 data points; chemical index of

alteration; and Si/Al ratio. Solid red lines are a low pass filtered curve on the carbonate $\delta^{18}O$ and $\delta^{13}C$ records.

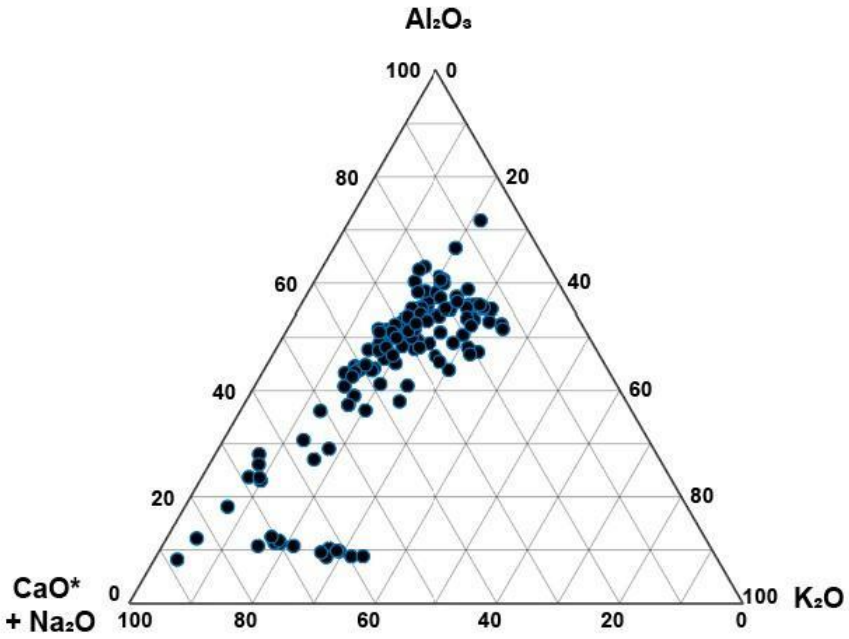

Figure S3. Ternary diagram for all clay samples with available data, showing the relative mole fractions of $CaO+Na_2O$, K_2O, and Al_2O_3.

Weathering Indices

The results of the CIA calculations are summarized in Figure S2 and shown in the time series in Figure S3. There does not appear to be a distinction between the lithologies in terms of the CIA values, with most plotting close to the Ca/Na and Al endmembers. There are, however, distinct shifts in the CIA value time series (Figure S3). From the base of the core, the CIA values stay below 40 until they reach the top of the halite beds where they then increase their weathered CIA value to ~60. The weathering indices stay high until the base of the thick ash at ~750 ka

where they drop to below 40. From the base of the ash to the top of the core the CIA values then increase gradually. We also plot Si/Al on Figure S3, which shows similar trends.